Strength-ductility synergy in an additively manufactured oxide dispersion strengthened Inconel 718 superalloy at 650 °C

Shengbin Dai[a, b, c], Jiangqi Zhu[c], Shun Wu[d], Martin Heilmaier[e], Yuman Zhu[a, b,*], Xingchen Yan[c,*], Aijun Huang[a, b]

[a] Monash Centre for Additive Manufacturing, 15-17 Normanby Rd, Notting Hill, VIC 3168, Australia
[b] Department of Materials Science and Engineering, Monash University, Clayton, VIC 3800, Australia
[c] Guangdong Academy of Sciences, Guangdong Institute of New Materials, National Engineering Laboratory for Modern Materials Surface Engineering Technology, The Key Lab of Guangdong for Modern Surface Engineering Technology, Guangzhou 510650, P. R. China
[d] Institute of Metallic Materials and Intelligent Manufacturing, School of lron and Steel, Soochow University, Suzhou 215137, P.R. China
[e] Institute for Applied Materials, Karlsruhe Institute of Technology, Engelbert-Arnold-Straße 4, 76131 Karlsruhe, Germany
Corresponding authors: yuman.zhu@monash.edu; yanxingchen@gdinm.com

Abstract

The retention of dislocation cellular patterns (DCPs) in laser powder bed fusion (LPBF) processed metals offers a novel pathway for achieving strength-ductility balance in high-temperature applications. This study innovatively combines oxide dispersion strengthening (ODS) with tailored heat treatment to stabilize DCPs in Inconel 718 (IN718) superalloys. Through strategic introduction of yttrium oxide (Y_2O_3) nanoparticles (average diameter $\approx$ 40 nm) and optimized solution treatments (1200°C for 5min/1h), we resolve the inherent conflict between residual stress elimination and microstructure preservation in LPBF-fabricated components. The 5-minute treated ODS alloy achieves exceptional synergy at 650°C: yield strength maintains 600 MPa while ductility increases 45% (from 20% to 29%) compared to as-built specimens. Crucially, our approach demonstrates two key innovations: 1) Y_2O_3 nanoparticles effectively pin dislocations movements, preserving DCPs structure against thermal coarsening; 2) Ultra-short heat treatment duration enables complete Laves phase dissolution without compromising dislocation network integrity. Microstructural analysis confirms that the stabilized DCPs-Y_2O_3 composite architecture facilitates simultaneous stress and strain accommodation. This work establishes a new paradigm for designing high-performance LPBF alloys through coupled process-microstructure optimization, particularly for aerospace components requiring elevated temperature mechanical stability.

Keywords

Laser powder bed fusion, nickel-based superalloys, oxide dispersion strengthened, dislocation cellular patterns, 650°C tensile properties, strength-ductility synergy.

1. Introduction

Nickel (Ni)-based superalloys are distinguished by their high melting points and excellent oxidation resistance, making them the primary materials used in the manufacture of combustion chambers and exhaust compartments in turbine engines [1]. A recent study has indicated that a 100 °C increase in the temperature of an aircraft engine's combustion chamber can potentially 10 times the thrust-to-weight ratio of the aircraft [2]. Consequently, raising the upper limit of the operating temperature for nickel-based high-temperature alloys is crucial for enhancing the thrust-to-weight ratio. Additionally, the increase in combustion chamber temperature imposes greater thermal impacts on the exhaust compartments. Therefore, nickel-based high-temperature alloys used in exhaust compartments, such as IN718, must also see improvements in their mechanical properties to meet these challenges.

Enhancing the high-temperature mechanical properties of Ni-based superalloys can be achieved through several methods. In nickel-based superalloys such as IN 718, a common strategy combines the introduction of alloying elements (e.g., Al, Ti, and Nb) with controlled aging treatments to generate dual-phase precipitation strengthening. The primary strengthening phases include both γ′ ($Ni_3(Al,Ti)$) and γ″ (Ni_3Nb) intermetallics [3–5]. These precipitates cooperatively enhance the yield strength of the alloy, with reported increments ranging from 400 to 500 MPa under standard service conditions [6]. However, as the operational temperature approaches 900 °C, the synergistic strengthening effect deteriorates markedly. This is attributed to the accelerated diffusion of Al, Ti, and Nb atoms into the matrix [7], which promotes both γ′ phase destabilization and γ″ phase dissolution. The latter phenomenon is particularly critical in IN 718 alloys, where γ″ precipitates dominate the mechanical performance but exhibit lower thermal stability than γ′ [4]. Alternatively, mechanical alloying can be used to incorporate oxide nanoparticles (typically yttrium oxide, Y_2O_3), leading to dispersion strengthening of the nickel-based alloys [8].

Oxide dispersion strengthening (ODS), for instance, the incorporation of 0.5 wt.% Y_2O_3 nanoparticles, provides a significant strength increase, e.g. by Orowan bypassing, of up to 120 MPa [9]. Despite this is usually lower than precipitation strengthening, this strengthening benefit persists at extreme temperatures exceeding 1000 °C, primarily due to the exceptional interfacial stability of Y_2O_3 dispersoids and the negligible diffusivity of its constituents in the metallic matrix. Their incoherent interface with the matrix, combined with a melting point (>2400 °C) far surpassing that of the alloy (~1300 °C), effectively suppresses coarsening and interfacial decohesion even approaching the matrix solidus temperature [9]. Such thermal insensitivity starkly contrasts with temperature-dependent γ′/γ″ precipitate degradation mechanisms described previously. However, the enhanced yield strength of

ODS nickel-based superalloys introduces dual challenges: (1) severe tool wear and subsurface micro-cracking during room-temperature machining (cutting forces >2× conventional alloys), and (2) inherent complexities in powder metallurgy (PM) processing—particularly the need for high-energy mechanical alloying (ball milling >20 h) and atmosphere-controlled consolidation (hot isostatic pressing at ~1200°C/150 MPa) to achieve nanoscale oxide dispersion [7]. Compared to cast/wrought counterparts, these combined factors increase manufacturing costs, as quantified in aerospace-grade ODS component production [10].

Laser powder bed fusion (LPBF) is an emerging additive manufacturing (AM) technology characterized by its ability to produce complex structures with net-shape [6,11,12]. This technology enables the accurate and rapid fabrication of intricate computer-designed geometries, addressing the challenges associated with machining complex internal cooling-systems features. As a result, a range of nickel-based superalloys, including ODS-Hastelloy X [13], ODS-IN625 [14], ODS-IN718 [15,16] and ODS-IN738LC [17], have been explored for production using LPBF. LPBF uniquely enables homogeneous oxide dispersion in ODS alloys despite traversing the molten state, as its rapid solidification kinetics (cooling rates $>10^4$ K/s) [18] suppress Stokes settling of oxide particles—a critical limitation in conventional casting where density differences between the melt (e.g., γ-Ni: ~8.9 g/cm³) and oxides (e.g., Y_2O_3: ~5.0 g/cm³) cause severe macro-segregation [19]. The LPBF-enabled dispersion homogeneity directly enhances high-temperature performance, elevating yield strength at 0.5 Tm by 18–22% compared to non-ODS variants under identical testing protocols [15].

The LPBF process is characterized by rapid solidification rates (~10^5–10^7 K/s) [18], which readily produce fine columnar dendritic cells. Due to the presence of alloying elements, the solidification process, dominated by constitutional supercooling, leads to significant segregation of elements such as Nb and Mo in the inter-dendritic regions. In certain nickel-based superalloys, such as IN718 and IN738LC, this segregation can result in the formation of hard and brittle Laves phases [15,16], which reduce the material's ductility. To homogenize the elemental distribution and dissolve the Laves phase, these alloys typically require subsequent solution heat treatment after printing [20,21].

Furthermore, the high-energy laser beam used in LPBF creates a molten pool, inducing impact stresses and thermal distortion that introduce significant plastic deformation into the material. These deformations are retained as geometrically necessary dislocations (GNDs), which ultimately form a dislocation cellular patterns (DCPs) structure [22–24]. The high residual stresses inherent in the printed material necessitate solution heat treatment.

Currently, the solution heat treatments for ODS nickel-based high-temperature alloys produced using LPBF technology are typically designed based on the properties of conventional wrought nickel-based high-temperature alloys. For instance, in the case of IN718, the standard solution heat treatment regime (as specified in AMS5662) involves holding the material at 971 °C for 1 hour, followed by air cooling.

However, at this temperature, the Laves phase does not fully dissolve [25]. Additionally, the DCPs only begin to decompose at temperatures around 1100 °C [24], indicating that the solution treatment temperature may need to be increased to achieve optimal microstructural homogenization.

However, existing studies [21,25,26] failed to reconcile the trade-off between stress relief and DCPs retention during post-AM heat treatments. To bridge this gap, we propose a novel solution heat treatment for ODS nickel-based high-temperature alloys fabricated by LPBF additive manufacturing technology. This heat treatment aims to restore a significant amount of ductility to the material without substantially compromising its yield strength, thereby achieving a strength-ductility synergy. The effectiveness of this treatment will be demonstrated through tensile properties measured at 650 °C, with corresponding microstructural changes characterized using scanning electron microscopy (SEM), transmission electron microscopy (TEM) and other characterizations.

2. Experimental

The gas-atomized IN718 powder was procured from Carpenter Company, while the yttria (Y_2O_3) nanoparticles were supplied by Aladdin Biochemical Technology Co., Ltd. The Y_2O_3 nanoparticles were distributed onto the IN718 powder using the electrostatic self-assembly (ESA) method, as detailed in our previous work [20]. The nominal addition of Y_2O_3 was 0.5 wt. %. The morphology of the Y_2O_3-doped IN718 powder is shown in **Fig. 1a**, **b**. The additive manufacturing system used was the D-150 GINM, specifically designed for laser powder bed fusion (LPBF) processing (**Table 1**). The printing parameters included a laser power of 170 W, a scanning speed of 1200 mm/s, a hatch distance of 60 μm, and a layer thickness of 20 μm. A 67° rotation between each layer was employed as the scanning strategy in this study. The three-dimensional orientations of the as-built specimens (IN718 and IN718-$0.5Y_2O_3$) are defined as the building direction (Z), horizontal direction (X), and normal direction (Y), where Z is parallel to the building direction, X is parallel to the roller's movement, and Y is perpendicular to the roller's movement. Through the optimization of alloy composition, processing parameters, and powder control in LPBF, cubic samples ($10 \times 10 \times 5$ mm^3) were created for microstructural investigation, while cylindrical samples (with a gauge length of 36 mm, a gauge diameter of 6 mm, and a grip segment diameter of 12 mm) were fabricated for tensile property measurements at 650 °C.

Table 1

Processing parameters of LPBF.

Laser power (W)	Scanning speed (mm/s)	Hatch distance (μm)	Layer thickness (μm)	Scanning strategy
170	1200	60	20	67° per layer

The heat treatment protocols employed were 1200 °C for 5 minutes and 1200 °C for 1 hour. The heat treatments were conducted using a TF1700 tube furnace under argon protection. The real-time temperature fluctuations were maintained within ± 10 °C, controlled by a Type-B thermocouple, with the temperature confirmed by a Type-K thermocouple. The as-built IN718 and IN718-0.5Y_2O_3 samples subjected to these two heat treatments are referred in **Table 2**.

Table 2

Summary of samples that experienced different solution heat treatments.

	Without Y_2O_3	With Y_2O_3
As-built	IN718	IN718-0.5Y_2O_3
1200 °C 5 min	1200 °C-5 min IN718	1200 °C-5 min IN718-0.5Y_2O_3
1200 °C 1 hour	1200 °C-1 hour IN718	1200 °C-1 hour IN718-0.5Y_2O_3

The phase analysis of the Y_2O_3-doped IN718 powder was conducted using X-ray diffraction (XRD) on a Rigaku Smartlab 9kW diffractometer, employing Cu-Kα radiation (40 kV/40 mA, λ = 1.5418 Å). The diffraction angle (2θ) was scanned over a range of 30–100° at a rate of 3°/min. The powder size distribution was measured using a Mastersizer 3000+. Bulk samples were prepared by grinding with sandpaper in the sequence of 320, 600, 1200, and 2500 grit, followed by polishing with 3 μm and 1 μm diamond suspensions, and a final polish using Struers OP-U NonDry oxide polishing suspension. The powder morphology and microstructures of the bulk samples were characterized using scanning electron microscopy (SEM) with FEI Quanta 3D FEGSEM and FEI Nova NanoSEM 450 FEGSEM instruments. The electron backscatter diffraction (EBSD) scans were performed with a step size of 0.2 μm. Nano-scale cellular structures, Y_2O_3 dispersion, and dislocations in the as-printed cubic samples and those subjected to solution treatment were characterized using transmission electron microscopy (TEM). TEM specimens were initially thinned mechanically to a thickness of 25 μm and subsequently prepared for final observations using a Gatan PIPS 695 for ion milling. The TEM analyses were conducted with an FEI Tecnai G2 T20 TWIN TEM (200 kV) and an FEI Tecnai G2 F20 S-TWIN TEM (200 kV). The FEI Tecnai G2 F20 S-TWIN TEM was equipped with an EDAX energy-dispersive X-ray spectroscopy (EDS) detector for determining the chemical composition of precipitates and was operated in scanning TEM (STEM) mode for detailed microstructural analysis. The particle size distribution of Y_2O_3 nanoparticles was statistically determined by averaging 15 individual measurements from representative regions of TEM images corresponding to the scale bars shown in **Fig. 3a**.

Tensile tests were conducted to evaluate the mechanical properties of the as-built and solution-treated samples along the horizontal direction (transverse specimens). These experiments were performed at

650 °C under quasi-static loading conditions (strain rate: 7×10^{-4} s^{-1}), following the ASTM E21-20 standard test method for elevated temperature tensile testing of metallic materials. The tests were carried out using a GOPOINT GJZX-A0004 universal tensile testing machine. For each group of as-built and solution-heat treated samples, three tensile specimens oriented along the horizontal direction (X) were tested.

3. Results

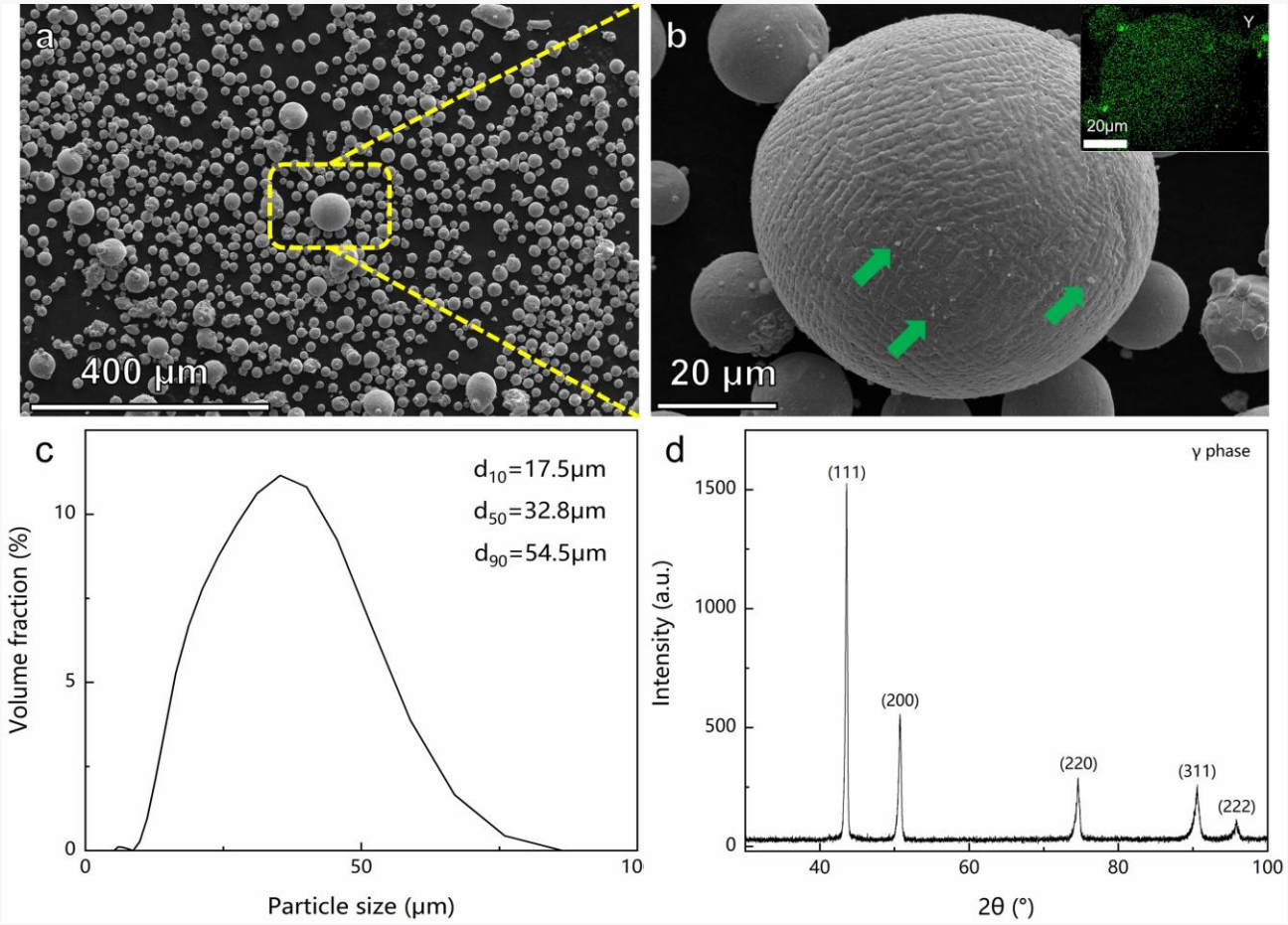

Fig. 1. Powder morphology and distribution of chemical composition. (a) SEM image of powder morphology of IN718 powder doped by Y_2O_3 nano-particles; (b) single IN718 particle with Y_2O_3 nanoparticle attached on the surface (inset is a Y element mapping image); (c) particle size distribution; (d) powder XRD results**.**

The IN718 powders utilized for LPBF exhibit a predominantly spherical morphology, interspersed with a few irregular particles, as illustrated in **Fig. 1a**. The doped Y_2O_3 nanoparticles are uniformly distributed on the surface of the IN718 particles, as shown in **Fig. 1b**. The particle size distribution of Y_2O_3 modified IN718 powder ranges from 18 to 55 μm, as depicted in **Fig. 1c**. Additionally, the γ phase is present within the powder composition, as evidenced in the results of powder XRD (**Fig. 1d**). The XRD signals of Y_2O_3 phase is not evident due to the low concentration.

Table 3

Chemical composition of the as-built IN718 and IN718-0.5Y_2O_3 samples (wt. %), measured by ICP-OES.

	Ni	Cr	Fe	Al	Ti	Mo	Nb	Y
IN718 as built	Bal.	17.46	19.07	0.53	1.01	3.05	5.52	/
0.5Y-IN718 as built	Bal.	17	17.62	0.49	0.91	3.16	6.47	0.18

The chemical compositions of as-built IN718 and IN718-0.5Y_2O_3 are tabulated and Y content is 0.18 wt. % (**Table 3**). The loss of Y is attributed to the following reasons: 1. Y_2O_3 nanoparticles are filtered by vacuum filter during powder preparation; 2. Y_2O_3 nanoparticles (5.01 g/cm^3 [27]) are lighter than liquid IN718 (7.39 g/cm^3 [28]) and are expected to flow on the surface of melting pool. During the LPBF processing, sputtering happened at the front edge of the melting pool [29] and part of Y_2O_3 nanoparticles were wasted.

3.1 Microstructures characterizations

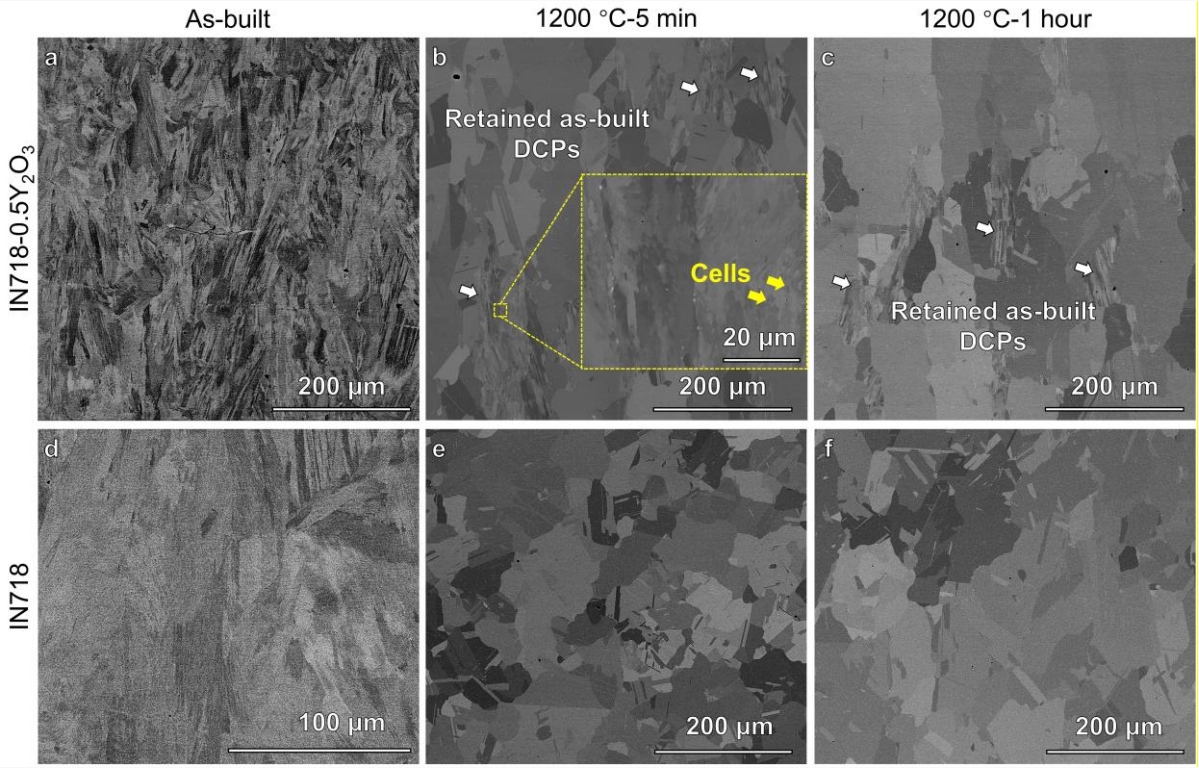

Fig. 2. Backscattered electron (BSE) images showing DCPs. (a) As-built IN718-0.5Y_2O_3 sample; retained DCPs in (b) the IN718-0.5Y_2O_3 sample after heat treatment at 1200 °C for 5 min, with the insert showing a higher-magnification BSE image of a DCP region, and (c) the IN718-0.5Y_2O_3 sample after 1200 °C for 1 h; (d) As-built IN718 sample; microstructures of (e) the IN718 sample after 1200 °C for 5 min and (f) the IN718 sample after 1200 °C for 1 h.

The microstructures of the as-built IN718-0.5 Y_2O_3 samples (**Fig. 2a**) consist DCPs. These DCPs form columnar cells, with their length oriented parallel to the building direction. After solution treatments at 1200 °C for 5 minutes and 1200 °C for 1 hour, both recrystallized grains and retained as-built DCPs are observed in the IN718-0.5 Y_2O_3 samples. The recrystallized grains also exhibit a columnar shape, with their length aligned parallel to the building direction (**Fig. 2b, c**).

DCPs are formed in the as-built IN718 samples (**Fig. 2d**). These DCPs exhibit a columnar shape, with their length oriented parallel to the building direction. After solution treatments at 1200 °C for 5 minutes and 1200 °C for 1 hour, the IN718 samples are predominantly composed of recrystallized grains. These recrystallized grains are irregular in shape and possess an approximate aspect ratio of 1:1 (**Fig. 2e, f**).

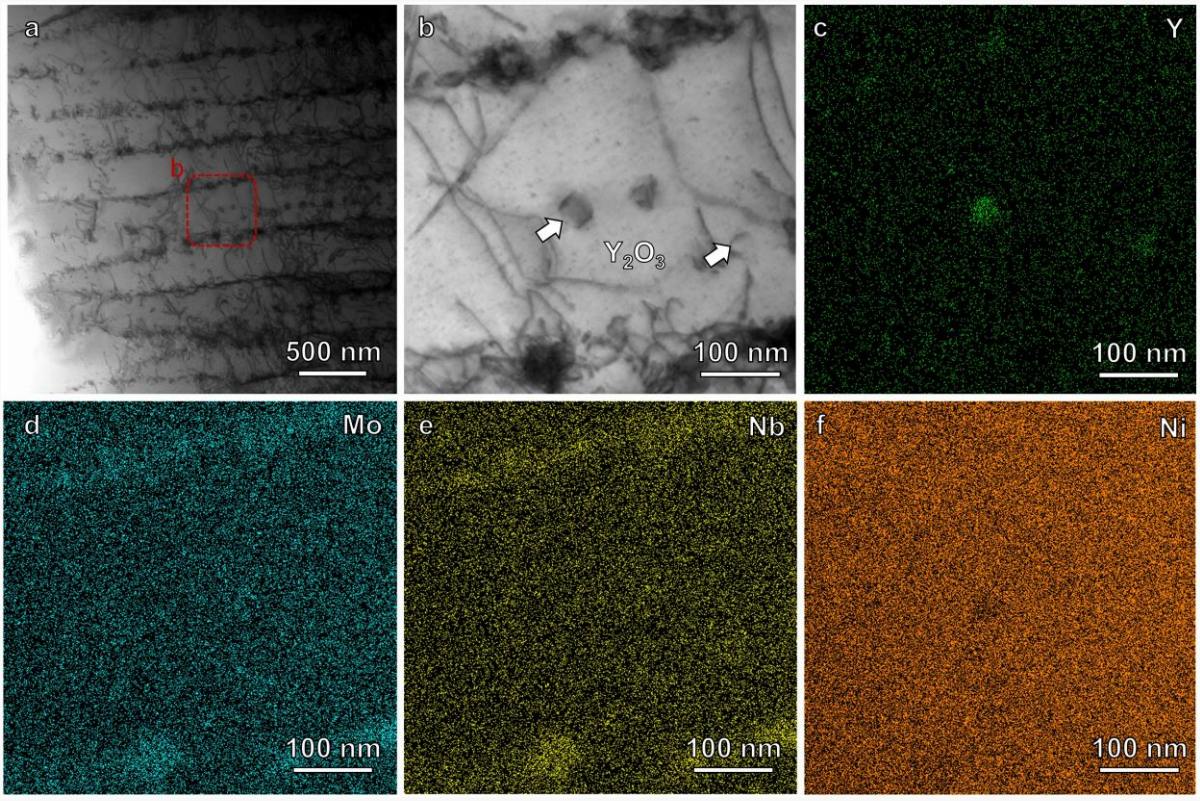

Fig. 3. (a) Dislocation cellular patterns in as-built IN718-0.5Y_2O_3 sample are characterized by bright field (BF)-STEM, (b) the magnified region; Distribution of chemical compositions of as-built IN718-0.5Y_2O_3 sample: (c) Y, (d) Mo, (e) Nb and (f) Ni.

The as-built IN718-0.5Y_2O_3 samples exhibit columnar cells, with an average width of 365 nm (**Fig. 3a**). These columnar cells are decorated with dislocations, and Y_2O_3 nanoparticles are observed within the matrix (**Fig. 3b**). The Y_2O_3 nanoparticles are spherical, with a diameter of approximately 40 nm. Additionally, Nb and Mo elements are found to segregate at the boundaries of the columnar cells.

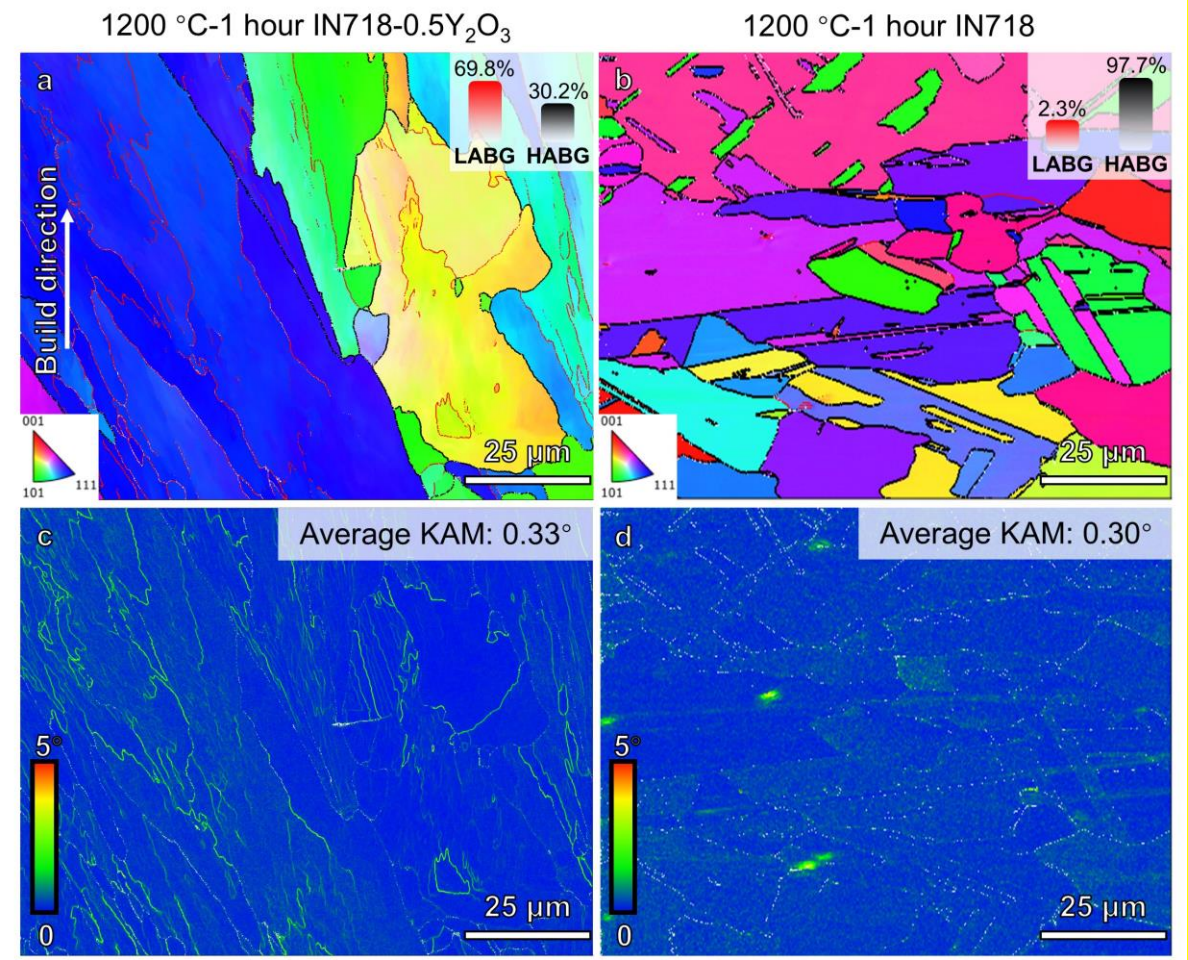

Fig. 4. IPF maps of (a) the IN718-0.5Y_2O_3 and (b) the IN718 samples annealed at 1200 °C for 1 h. Inset charts show the quantitative fractions of low-angle grain boundaries (LAGBs, red lines) and high-angle grain boundaries (HAGBs, black lines). Kernel average misorientation (KAM) maps of (c) the IN718-0.5 Y_2O_3 and (d) the IN718 samples under the same heat treatment, with insets displaying the average KAM values of the corresponding regions.

In both **Fig. 4a** and **Fig. 4b**, LAGBs are represented by red lines, defined by grain misorientation angles ranging from 2° to 15°. HAGBs are indicated by black lines, with misorientation angles exceeding 15°. **Fig. 4a** illustrates a region of retained DCPs in the IN718-0.5Y_2O_3 sample after a 1200 °C, 1-hour solution treatment, where LAGBs predominate. In contrast, **Fig. 4b** shows a region of IN718 subjected to the same treatment, displaying recrystallized grains dominated by HAGBs. The lattice misfit along the LAGBs in the region of retained DCPs is depicted in **Fig. 4c**, highlighting the origin of geometrically necessary dislocations (GNDs) [30]. No evident lattice misfit is observed in the recrystallized grains, as shown in **Fig. 4d**.

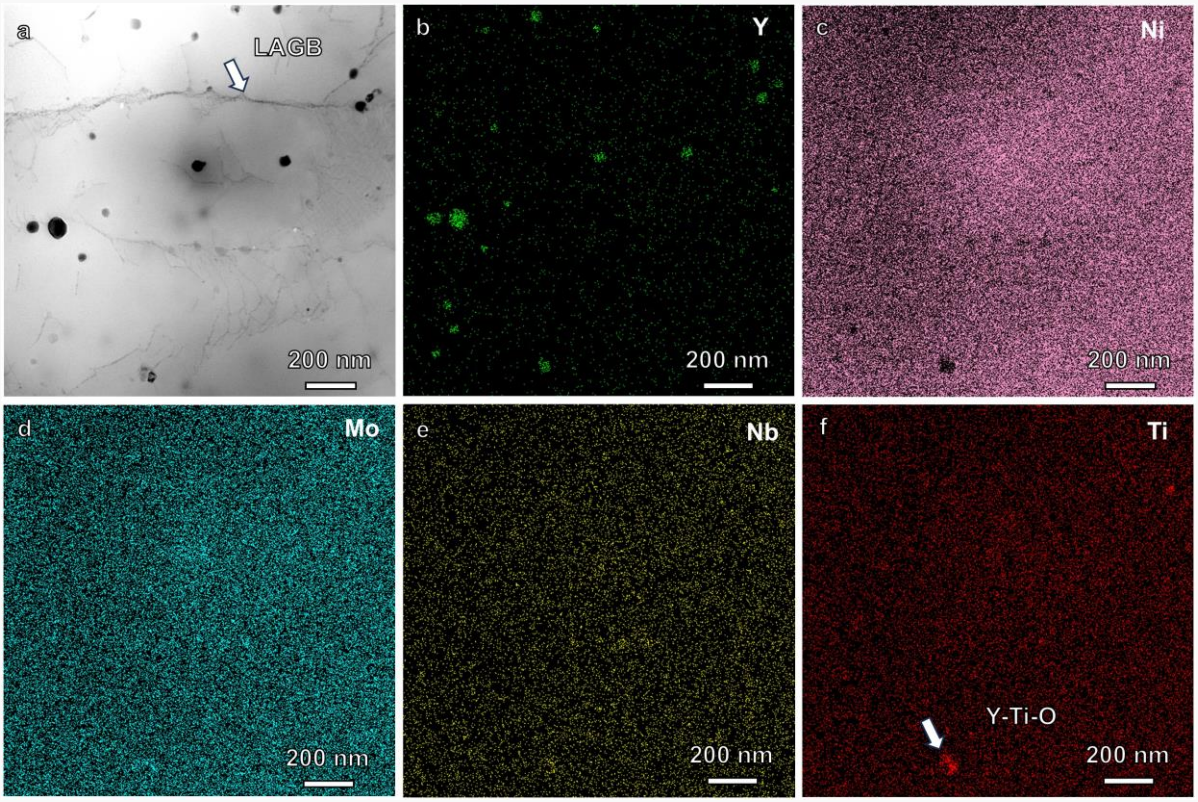

Fig. 5. STEM-EDS mappings of 1200 °C-1 hour IN718-0.5Y_2O_3 tensile sample. (a) A BF image; (b) Y distribution; (c) Ni distribution; (d) Mo distribution; (e) Nb distribution; (f) Ti distribution.

The primary difference between IN718 and IN718-0.5Y_2O_3 lies in the presence of Y_2O_3 and its interactions with LAGBs as observed in the results presented in **Fig. 4**. A similar microstructure is observed in the IN718-0.5Y_2O_3 samples subjected to tensile testing at 650 °C (**Fig. 5a** and **5b**), where the Y_2O_3 particles are aligned along the LAGBs. The distributions of Mo and Nb are homogeneous, indicating complete dissolution of the Laves phase. However, a slight segregation of Ti is identified by STEM-EDS mapping, exhibiting a rectangular shape distinct from the round Y_2O_3 particles. This Ti segregation in IN718 after solution treatment is typically considered as Y-Ti-O chemical compounds (**Fig. 5f**), similar to those reported in ODS steels [31].

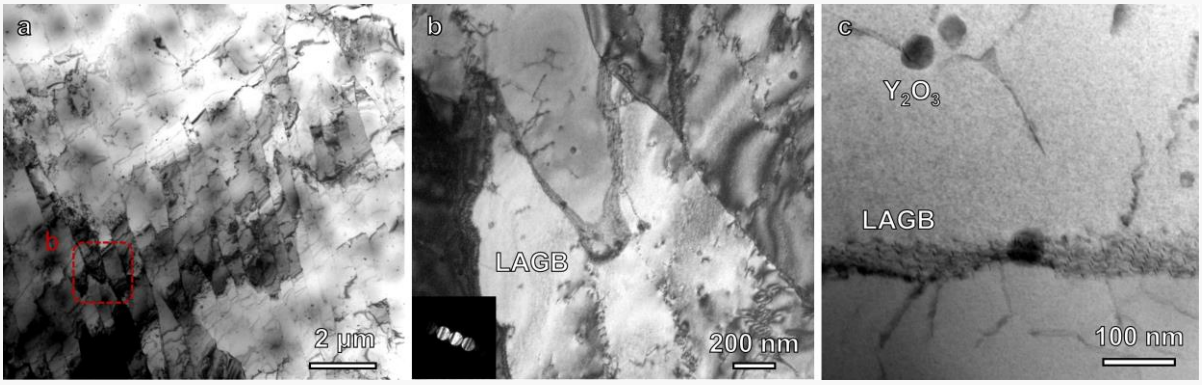

Fig. 6. (a) BF-TEM image of microstructure of 1200 °C-1hour IN718-0.5Y_2O_3 sample for 650 °C tensile test; (b) magnified region, insert is convergent beam electron diffraction (CBED) pattern; (c) BF-STEM image of the interaction between Y_2O_3 nanoparticles with LAGBs and dislocations.

Columnar cells are clearly visible in the matrix of the IN718-0.5Y_2O_3 sample after a 1-hour solution treatment at 1200 °C (**Fig. 6a**). These cells retain the same columnar morphology observed in the as-built IN718-0.5Y_2O_3, but the continuous Laves phases previously formed at the cell boundaries have completely dissolved into the matrix. The average width of the columnar cells is measured to be 365 nm, closely matching that of the as-built sample. Under the g = <002> three-beam condition, dislocations with a Burgers vector of b = <011>(111) are visible (**Fig. 6b**), consistent with the invisibility criterion [32,33]. These dislocations are impeded by Y_2O_3 nanoparticles. LABGs are composed of twisted dislocations, which are also pinned by Y_2O_3 (**Fig. 6c**). To some extent, the Y_2O_3 nanoparticles assume the role previously played by the Laves phase and the segregation of Nb and Mo in the as-built IN718-0.5Y_2O_3. The Y_2O_3 nanoparticles help to retain the DCPs even after the solution treatment.

3.2 650 °C tensile properties

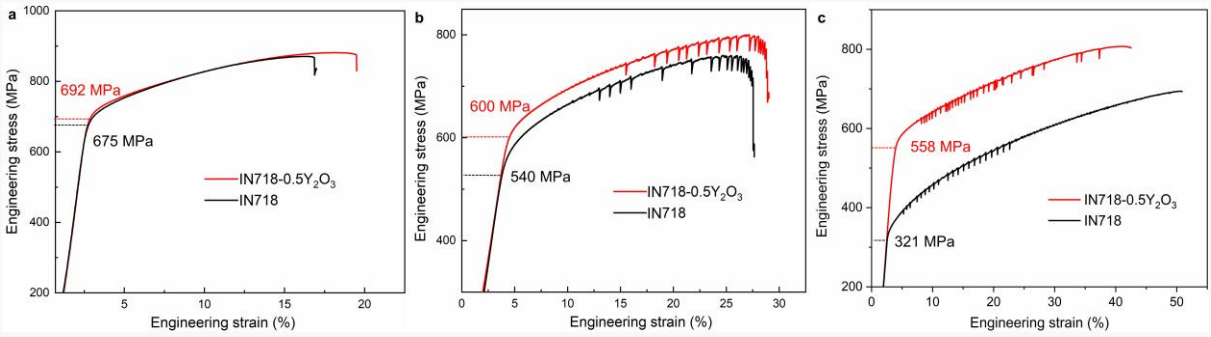

Fig. 7. (a) 650°C tensile properties of as-built IN718-0.5Y_2O_3 and IN718 samples; (b) 650°C tensile properties of 1200°C-5 min IN718-0.5Y_2O_3 and IN718 samples; (c) 650°C tensile properties of 1200°C-1 hour IN718-0.5Y_2O_3 and IN718 samples.

The synergistic strengthening-ductility balance of the ODS variant is highlighted through 650°C tensile testing. In the as-built condition, IN718-0.5Y_2O_3 exhibits comparable yield strength to IN718

(692 vs. 675 MPa, **Fig. 7a**), yet achieves 20% strain versus 18% for the baseline (**Table 4**)—a 26% ductility enhancement without significant strength compromise. This advantage suggests that post-solution heat treatment: after 1 hour at 1200°C, the ODS alloy retains 558 MPa yield strength (85% of its initial value) versus 321 MPa for IN718 (65% retention), paired with 32% strain compared to 40% for the non-ODS alloy. Both alloys after solution heat treatment display the Portevin–Le Chatelier (PLC) effect (flow stress serrations in **Fig. 7b–c**) **[34]**.

Table 4

Summary of tensile properties at 650 °C for IN718-0.5Y_2O_3 and IN718 in different conditions. (Three tensile samples were tested for each condition).

	Yield strengths (MPa)	Ultimate tensile strengths (MPa)	Strain to failure (%)
IN718 as built	675±7	871±10	18±2
IN718-0.5Y_2O_3 as built	692±9	882±6	20±4
1200 °C-5 min IN718	540±3	759±5	26±1
1200 °C-5 min IN718-0.5Y_2O_3	600±8	801±3	29±2
1200 °C-1 hour IN718	321±2	694±3	50±2
1200 °C-1 hour IN718-0.5Y_2O_3	558±6	807±4	42±3

Fractographic and microstructural analyses were conducted on IN718 and IN718-0.5Y_2O_3 alloys in both CBEDas-built and heat-treated conditions (1200 °C for 5 min, **Fig. 8**). The as-built IN718-0.5Y_2O_3 sample exhibited a classic ductile fracture surface with numerous dimples, indicative of microvoid coalescence and significant plastic deformation. In contrast, the as-built IN718 sample without Y_2O_3 showed a mixed fracture mode, characterized by dendritic solidification features and partial tearing ridges, suggesting inhomogeneous mechanical response due to microsegregation. After heat treatment, the IN718-0.5Y_2O_3 sample maintained a ductile fracture mode with uniformly distributed fine dimples. This correlates with the formation of dislocation cell structures observed in the microstructure, which enhance strain hardening and promote uniform plastic deformation. Conversely, the heat-treated IN718 sample exhibited a relatively smooth fracture surface with fewer and larger voids, indicative of a reduced ductility. Microstructural examination revealed the presence of annealing twins rather than dislocation cell structures, suggesting limited plastic accommodation during deformation. The absence of dislocation cell networks and the presence of brittle features imply that grain boundary softening or

premature decohesion might dominate the fracture process in the heat-treated IN718 alloy. Overall, the addition of Y_2O_3 not only refines the fracture morphology but also promotes favorable substructure evolution during heat treatment, thereby enhancing ductility and fracture resistance.

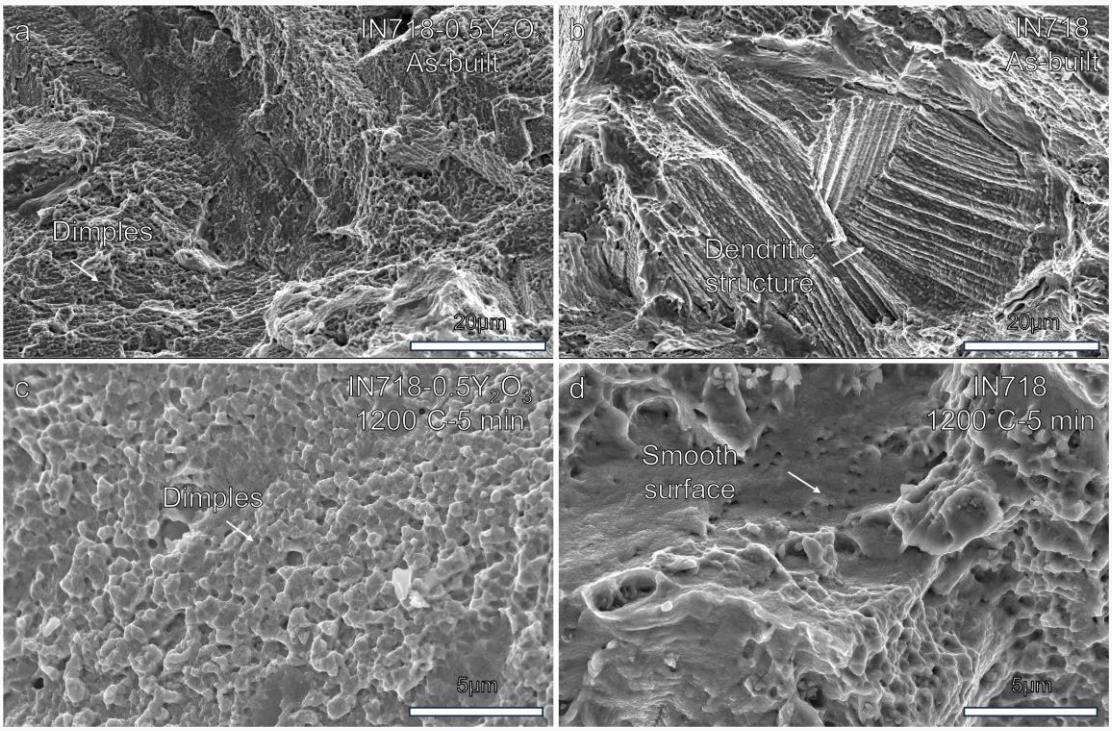

Fig. 8. Fractography of 650 °C tensile samples: (a) IN718-0.5Y_2O_3 as-built; (b) IN718 as-built; (c) IN718-0.5Y_2O_3 after 5 min solution heat treatment; (d) IN718 after 5 min solution heat treatment.

4. Discussion

4.1 Strengthening mechanisms

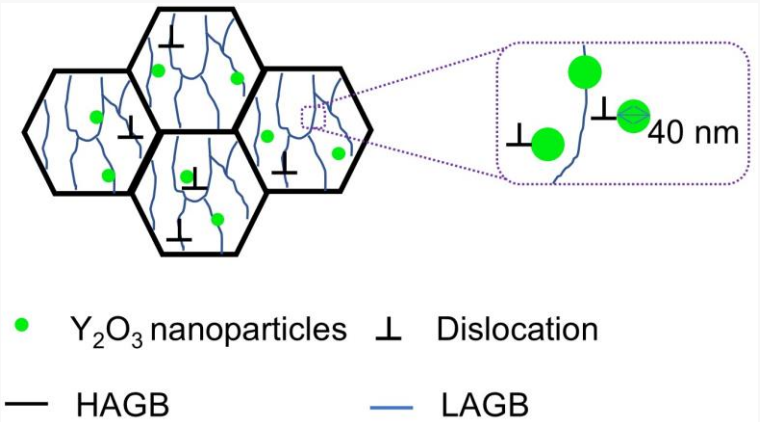

Fig. 9. Schematic summary of the strengthening mechanisms that may operate in IN718-0.5Y_2O_3 samples.

The strengthening mechanisms contributing to the yield strength of IN718-0.5Y_2O_3 can be attributed to dispersion (second-phase) strengthening, dislocation strengthening, and grain boundary

strengthening (**Fig. 9**). The Y_2O_3 nanoparticles are uniformly distributed within the matrix of IN718-0.5Y_2O_3, where they interact with dislocations and LAGBs. The presence of Y_2O_3 nanoparticles can effectively hinder the movement of dislocations, leading to the formation of curved dislocation features (**Fig. 6**). At 650 °C (0.5T_m of IN718), dislocation dynamics transition to a dual-mechanism regime: (i) thermally assisted climb over Y_2O_3 nanoparticles becomes achievable via enhanced vacancy diffusion [35], while (ii) Orowan bypassing persists as the dominant strengthening mechanism below 700 °C. This temperature-dependent interplay between climb and bypass activity – validated through post-test TEM analysis in [35] – rationalizes the retention of high yield strength (558 MPa) despite the onset of dynamic recovery at 0.5T_m (**Fig. 7c**). Despite this, the Y_2O_3 nanoparticles continue to impede dislocation movement, making Orowan bypassing the primary strengthening mechanism associated with these nanoparticles.

The formation of DCPs, a metastable substructure ubiquitously observed in LPBF-processed alloys [22,36], emerges from coupled rapid solidification and deformation induced by the thermal cycling. Specifically, (i) nanosecond-scale melt pool solidification under cooling rates exceeding 10^6 K/s generates dense dislocation tangles, while (ii) successive thermal cycles induce non-uniform plasticity that reorganizes dislocations into low-energy cell walls (**Fig. 6a**). This dual driving mechanism explains the geometry-dependent DCP refinement in Ni-superalloys versus steel variants [23,24,37], quantified through KAM mapping in **Fig.4c**. Rapid solidification is typically attributed to constitutional supercooling, where solute elements segregate in the interdendritic regions. This phenomenon is observed in both as-built IN718 [16,21] and IN718-0.5Y_2O_3 (**Fig. 4**), with Nb and Mo alloying elements are concentrating in these regions. Thermal distortion, on the other hand, involves plastic deformation that generates dislocations. Dislocations preferentially segregate to chemically stabilized low-energy zones, particularly solute-enriched dendritic boundaries, via Cottrell-type solute-dislocation interactions [38,39]. The presence of DCPs has been confirmed in both as-built IN718-0.5Y_2O_3 (**Fig. 2a**) and IN718 (**Fig. 2d**).

The differences between IN718 and IN718-0.5Y_2O_3 become evident after a 5-minute solution treatment at 1200 °C. In the IN718 sample, DCPs disappear (**Fig. 2e**), whereas in the IN718-0.5Y_2O_3 sample, they are retained (**Fig. 2b**). Although recrystallization occurs in both materials, the recrystallization kinetics in IN718-0.5Y_2O_3 are notably slower. Even after a 1-hour solution treatment at 1200 °C, the DCPs persist in IN718-0.5Y_2O_3 (**Fig. 2c**). The Mo and Nb segregations observed in the interdendritic regions of as-built IN718-0.5Y_2O_3 samples disappear after a 1-hour solution treatment at 1200 °C (**Fig. 5d** and **5e**). The dispersed Y_2O_3 nanoparticles exert dual strengthening effects through LAGB stabilization and dynamic dislocation pinning: the primary driving force for the segregation of Y_2O_3 nanoparticles to LAGBs is the reduction of interfacial energy. This is a common mechanism in polycrystalline materials where solute atoms or nanoparticles migrate to grain boundaries to minimize the system's overall energy, impeding LAGB migration and refining the substructure [40,41]. This

stabilization reduces the effective dislocation glide distance (λ), enhancing yield strength via a modified Hall-Petch relationship ($\Delta\sigma \propto \lambda^{-1/2}$)[42]; During plastic deformation, rigid nanoparticles act as Orowan bypass inclusion, as confirmed by TEM observation of dislocations which are looping around Y_2O_3 particles (**Fig. 6c**). Critically, this nanoscale dispersion synergistically retains uniform ductility by delaying void nucleation at stabilized LAGBs, evidenced by dimple density reduction in fracture surfaces (**Fig. 8c vs. Fig. 8d**).

4.2 Heat treatment time vs. yield strengths

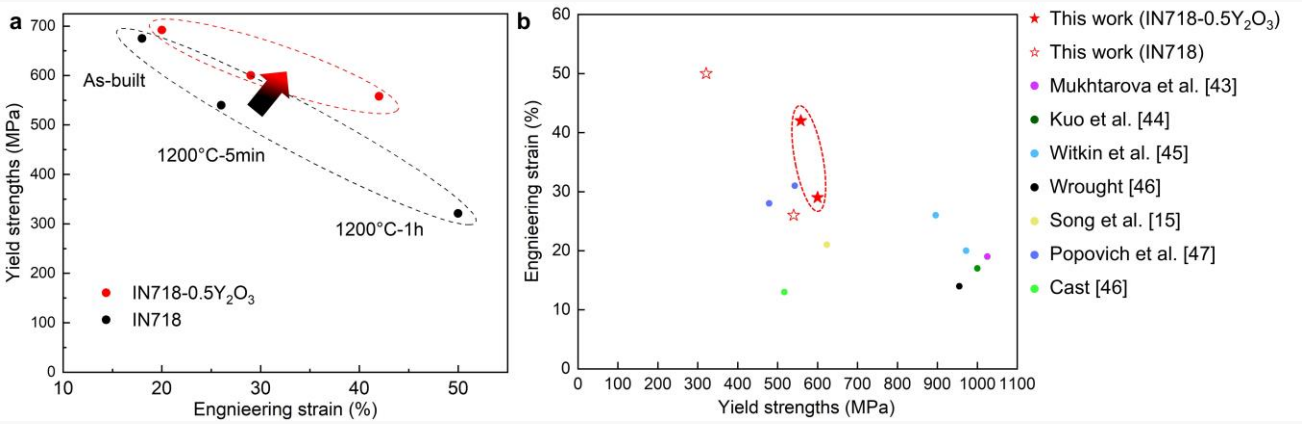

Fig. 10. (a) Tensile properties at 650 °C of IN718 and IN718-0.5Y_2O_3 as a function of solution treatment time; (b) A summary of engineering strain versus yield strength for various LPBF-fabricated IN718 alloys tested at 650 °C, including this work, as-built IN718, HIP-treated IN718, and solution-treated plus aged IN718, along with data for wrought and cast IN718. [15,43–47].

The yield strength at 650 °C decreases with increasing solution treatment time for both IN718 and IN718-0.5Y_2O_3, while the strain increases significantly (**Table 4**). This represents a trade-off between yield strength and strain that can be manipulated by adjusting the solution treatment duration. Notably, the yield strength of IN718-0.5Y_2O_3 at 650 °C decreases at a slower rate compared to its IN718 counterpart. In other word, the relatively high-level 650 °C tensile properties of IN718-0.5Y_2O_3 can be preserved longer after 1200 °C solution treatment, compared with IN718 (**Fig. 10a**). Specifically, the 650 °C yield strength of the IN718 sample subjected to a 1200 °C, 1-hour solution treatment decreases by 37% compared to the 1200 °C, 5-minute IN718 sample (**Fig. 10a**), despite the 1200 °C, 1-hour IN718 showing the highest strain among all conditions. The 1200 °C, 5-minute IN718-0.5Y_2O_3 sample maintains an ideal balance between yield strength and strain. The fraction of retained DCPs in the 1200 °C, 5-minute and 1200 °C, 1-hour IN718-0.5Y_2O_3 samples is correlated with yield strength. In the as-built IN718-0.5Y_2O_3, the DCPs are considered to fully fill the microstructure. This fraction decreases to 27% in the 1200 °C, 5-minute IN718-0.5Y_2O_3 sample and further to 20% in the 1200 °C, 1-hour IN718-0.5Y_2O_3 sample. Compared with other as-built or HIP-treated IN718 (Fig. 10b), our work stands

out for its excellent balance between strength and ductility. With a carefully designed ageing treatment, the yield strength of the IN718-0.5Y_2O_3 sample can be further increased to approximately 1000 MPa.

The temperature of 1200 °C is close to the melting point of IN718 (~1400 °C), and the solution treatment at this temperature, the 650 °C yield strength of the as-built samples decreases. This reduction can be attributed to two primary factors: first, a decrease in the GND density, owing to the recovery of dislocations initially introduced by thermal deformation during the printing process; and second, the onset of recrystallization and rapid growth of newly formed grains, leading to coarser grains with fewer boundaries. This reduced capacity to impede dislocation motion results in a lower 650 °C yield strength compared to the as-built samples.

However, if the 650 °C yield strength and strain values of the as-built samples are set as 100% reference values, it is observed that IN718 samples reinforced with Y_2O_3 nanoparticle dispersion retain higher yield strengths over prolonged solution treatment time and exhibit increased ductility. This characteristic provides a broader window for high-temperature solution heat treatments in yttrium oxide-reinforced IN718, suggesting that this material is better suited for extreme temperature environments than standard IN718.

Analysis of backscattered and transmission electron microscopy images of IN718-0.5Y_2O_3 compared to IN718 indicates that the superior high-temperature mechanical properties of yttrium oxide-diffusion-reinforced IN718 are due to (1) the uniform dispersion of yttrium oxide nanoparticles within the IN718 matrix, and (2) the retention of the DCP structure. Notably, the greater the proportion of these DCP structures (e.g., in 1200 °C-5 min solution-treated samples), the higher the yield strength. Moreover, high-temperature solution treatment enhances ductility, resulting in an optimal synergy of strength and ductility in these alloys.

5. Conclusions

To enhance the high-temperature performance of IN718 at its service condition (650 °C), 0.5 wt.% Y_2O_3 nanoparticles were introduced to activate dual strengthening pathways. Solution heat treatment at 1200 °C (5 min and 1 h), the IN718-0.5Y_2O_3 system exhibits superior thermal stability, evidenced by a mitigated yield strength degradation rate. The key findings from this study are summarized as follows:

1. Direct dispersion strengthening: Y_2O_3 nanoparticles obstruct dislocation motion via thermally stable Orowan bypassing;
2. Indirect substructure stabilization: Nanoparticles pin low-angle grain boundaries (LAGBs) through interfacial segregation, which retards dynamic recovery and preserves dislocation-cell structures (DCPs).
3. A strength-ductility synergy at 650 °C in IN718-0.5Y_2O_3 can be achieved by optimizing the solution treatment conditions.

However, quantitating the strengths contribution of two mechanisms— also highlighted in Hazzledine's framework [48]—is still difficult.

Acknowledgements

The authors gratefully acknowledge the scientific and technical assistance at the Monash Centre for Additive Manufacturing (MCAM) and Monash Centre for Electron Microscopy (MCEM) as a Node of Microscopy Australia. This research used equipment funded by Australian Research Council grants: FEI Tecnai G2 F20 S-TWIN FEGTEM (LE110100223) and Thermo Fisher Scientific Helios 5 UX FIBSEM (LE200100132). S.B. Dai and S. Wu wish to thank the financial support from the Monash Graduate Scholarship. The authors would also gratefully acknowledge the National K&D Program (2022YFC2406000), National Natural Science Foundation of China (52405347), Guangdong Basic and Applied Basic Research Foundation (2022B1515250004, 2024A1515011024), Guangdong Provincial Key R&D Programme (2023B0909020004), Guangdong Special Support Program for Young Top-Notch Talents in Science and Technology Innovation (2023TQ07Z559), Guangdong province Science and Technology Plan Projects (2023B1212120008, 2023B1212060045), Guangdong Academy of Science Projects (2022GDASZH-2022010107 and 2021GDASYL-20210102005), the Guangzhou Science and Technology Project (2025A04J3920).

Graphical abstract

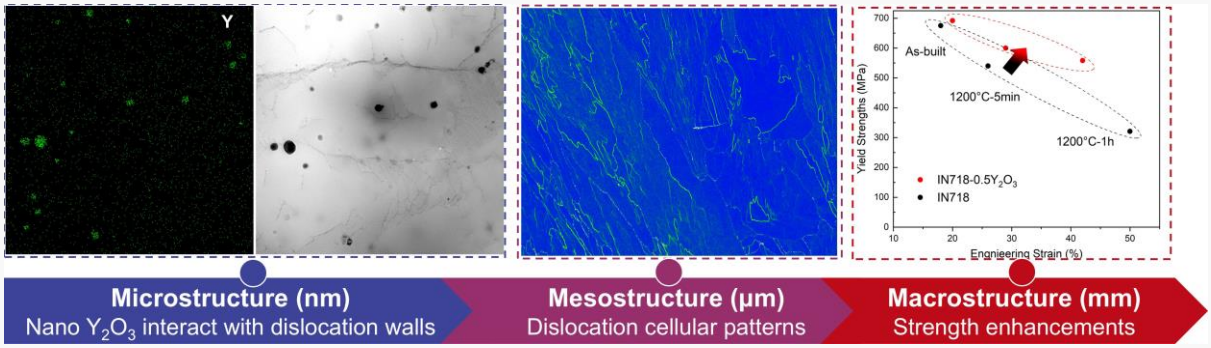

References

[1] R.C. Reed, The Superalloys: Fundamentals and Applications, Cambridge University Press, Cambridge, 2006. https://doi.org/10.1017/CBO9780511541285.

[2] L.R. Jenkinson, P. Simpkin, D. Rhodes, Civil Jet Aircraft Design, American Insitute of Aeronautics and Astronautics, USA, 1999.

[3] O. Adegoke, J. Andersson, H. Brodin, R. Pederson, Review of laser powder bed fusion of gamma-prime-strengthened nickel-based superalloys, Metals 10 (2020) 996–1022. https://doi.org/10.3390/met10080996.

[4] P.A. Buffat, I. Alexandrou, A. Czyrska-Filemonowicz, Composition and element distribution mapping of gamma' and gamma'' phases of inconel 718 by high-resolution scanning transmission electron microscopy and X-ray energy-dispersive spectrometry, Materials (Basel) 17 (2024) 594–612. https://doi.org/10.3390/ma17030594.

[5] H. Zhang, K. Chen, S. Lin, R. Fu, B. Zhang, J. Ding, Z. Feng, X. Huang, E. Ma, Recovery facilitated by interphase boundary motion circumvents recrystallization in superalloy single crystals, Materials Research Letters 12 (2024) 180–189. https://doi.org/10.1080/21663831.2024.2312146.

[6] S. Sanchez, P. Smith, Z. Xu, G. Gaspard, C.J. Hyde, W.W. Wits, I.A. Ashcroft, H. Chen, A.T. Clare, Powder bed fusion of nickel-based superalloys: A review, Int. J. Mach. Tools Manuf. 165 (2021) 103729–103807. https://doi.org/10.1016/j.ijmachtools.2021.103729.

[7] M.S.A. Karunaratne, P. Carter, R.C. Reed, On the diffusion of aluminium and titanium in the ni-rich ni–al–ti system between 900 and 1200°C, Acta Materialia 49 (2001) 861–875. https://doi.org/10.1016/S1359-6454(00)00390-6.

[8] J. S. Benjamin, Dispersion strengthened superalloys by mechanical alloying, Metallurgical Transactions 1 (1970) 2943–2951. https://doi.org/10.1007/BF03037835.

[9] C. Kenel, A. De Luca, S.S. Joglekar, C. Leinenbach, D.C. Dunand, Evolution of Y2O3 dispersoids during laser powder bed fusion of oxide dispersion strengthened Ni-Cr-Al-Ti γ/γ' superalloy, Additive Manufacturing 47 (2021) 102224. https://doi.org/10.1016/j.addma.2021.102224.

[10] F. Bergner, I. Hilger, J. Virta, J. Lagerbom, G. Gerbeth, S. Connolly, Z. Hong, P.S. Grant, T. Weissgärber, Alternative Fabrication Routes toward Oxide-Dispersion-Strengthened Steels and Model Alloys, Metall Mater Trans A 47 (2016) 5313–5324. https://doi.org/10.1007/s11661-016-3616-2.

[11] E. Hosseini, V.A. Popovich, A review of mechanical properties of additively manufactured inconel 718, Additive Manufacturing 30 (2019) 100877. https://doi.org/10.1016/j.addma.2019.100877.

[12] J.O. Milewski, Additive Manufacturing Metal, the Art of the Possible, in: J.O. Milewski (Ed.), Additive Manufacturing of Metals: From Fundamental Technology to Rocket Nozzles, Medical

Implants, and Custom Jewelry, Springer International Publishing, Cham, 2017: pp. 7–33. https://doi.org/10.1007/978-3-319-58205-4_2.

[13] X. Cheng, Y. Zhao, Z. Qian, J. Wu, J. Dong, Z. Ma, Y. Liu, Crack elimination and mechanical properties enhancement in additive manufactured hastelloy X via in-situ chemical doping of Y2O3, Materials Science and Engineering: A 824 (2021) 141867. https://doi.org/10.1016/j.msea.2021.141867.

[14] M. Li, L. Wang, H. Yang, S. Zhang, X. Lin, W. Huang, Microstructure and mechanical properties of Y2O3 strengthened inconel 625 alloy fabricated by selective laser melting, Materials Science and Engineering: A 854 (2022) 143813. https://doi.org/10.1016/j.msea.2022.143813.

[15] Q. Song, Y. Zhang, Y. Wei, X. Zhou, Y. Shen, Y. Zhou, X. Feng, Microstructure and mechanical performance of ODS superalloys manufactured by selective laser melting, Opt. Laser Technol. 144 (2021) 107423–107433. https://doi.org/10.1016/j.optlastec.2021.107423.

[16] D.N. Luu, W. Zhou, S.M.L. Nai, Influence of nano-Y2O3 addition on the mechanical properties of selective laser melted Inconel 718, Materials Science and Engineering: A 845 (2022) 143233. https://doi.org/10.1016/j.msea.2022.143233.

[17] C. Guo, Z. Yu, X. Hu, G. Li, F. Zhou, Z. Xu, S. Han, Y. Zhou, R.M. Ward, Q. Zhu, Y2O3 nanoparticles decorated IN738LC superalloy manufactured by laser powder bed fusion: Cracking inhibition, microstructures and mechanical properties, Composites Part B: Engineering 230 (2022) 109555. https://doi.org/10.1016/j.compositesb.2021.109555.

[18] V. Bhavar, P. Kattire, V. Patil, S. Khot, K. Gujar, R. Singh, A review on powder bed fusion technology of metal additive manufacturing, Additive Manufacturing Handbook (2017) 251–253. https://doi.org/10.1201/9781315119106-15.

[19] L. Nastac, CFD Modeling of Macro-segregation and Shrinkage During Solidification of Superalloy Castings, ISIJ International 50 (2010) 1829–1834. https://doi.org/10.2355/isijinternational.50.1829.

[20] S. Dai, J. Zhu, X. Yan, S. Wu, Y. Liu, X. Gao, H. Fraser, P. Hodgson, Y. Zhu, M. Heilmaier, A. Huang, Unique yttria nanoparticle strengthening in an inconel 718 superalloy fabricated by additive manufacturing, Advanced Materials Technologies 9 (2023). https://doi.org/10.1002/admt.202301421.

[21] S. Wu, H.Z. Peng, X. Gao, P.D. Hodgson, H.Y. Song, Y.M. Zhu, Y. Tian, A.J. Huang, Improving creep property of additively manufactured inconel 718 through specifically-designed post heat treatments, Mater. Sci. Eng., A 857 (2022) 144047–144058. https://doi.org/10.1016/j.msea.2022.144047.

[22] M. He, H. Cao, Q. Liu, J. Yi, Y. Ni, S. Wang, Evolution of dislocation cellular pattern in inconel 718 alloy fabricated by laser powder-bed fusion, Additive Manufacturing 55 (2022) 102839. https://doi.org/10.1016/j.addma.2022.102839.

[23] K.M. Bertsch, G. Meric De Bellefon, B. Kuehl, D.J. Thoma, Origin of dislocation structures in an additively manufactured austenitic stainless steel 316L, Acta Materialia 199 (2020) 19–33. https://doi.org/10.1016/j.actamat.2020.07.063.

[24] T. Voisin, J.-B. Forien, A. Perron, S. Aubry, N. Bertin, A. Samanta, A. Baker, Y.M. Wang, New insights on cellular structures strengthening mechanisms and thermal stability of an austenitic stainless steel fabricated by laser powder-bed-fusion, Acta Mater. 203 (2021) 116476–116493. https://doi.org/10.1016/j.actamat.2020.11.018.

[25] L. Emanuelli, F. Deirmina, M. Pellizzari, Heat treatment behaviour of IN718 superalloy fabricated by laser-powder bed fusion, Materials Characterization 199 (2023) 112788. https://doi.org/10.1016/j.matchar.2023.112788.

[26] G.H. Cao, T.Y. Sun, C.H. Wang, X. Li, M. Liu, Z.X. Zhang, P.F. Hu, A.M. Russell, R. Schneider, D. Gerthsen, Z.J. Zhou, C.P. Li, G.F. Chen, Investigations of γ′, γ″ and δ precipitates in heat-treated Inconel 718 alloy fabricated by selective laser melting, Materials Characterization 136 (2018) 398–406. https://doi.org/10.1016/j.matchar.2018.01.006.

[27] M.R. Mattli, R.A. Shakoor, P.R. Matli, A.M. Amer Mohamed, Microstructure and Compressive Behavior of Al–Y2O3 Nanocomposites Prepared by Microwave-Assisted Mechanical Alloying, Metals 9 (2019) 414. https://doi.org/10.3390/met9040414.

[28] H.P. Wang, C.H. Zheng, P.F. Zou, S.J. Yang, L. Hu, B. Wei, Density determination and simulation of Inconel 718 alloy at normal and metastable liquid states, Journal of Materials Science & Technology 34 (2018) 436–439. https://doi.org/10.1016/j.jmst.2017.10.014.

[29] Y. Wang, W. Guo, Y. Xie, H. Li, C. Zeng, M. Xu, H. Zhang, In-situ monitoring plume, spattering behavior and revealing their relationship with melt flow in laser powder bed fusion of nickel-based superalloy, Journal of Materials Science & Technology 177 (2024) 44–58. https://doi.org/10.1016/j.jmst.2023.07.068.

[30] C. Moussa, M. Bernacki, R. Besnard, N. Bozzolo, About quantitative EBSD analysis of deformation and recovery substructures in pure tantalum, IOP Conference Series: Materials Science and Engineering 89 (2015) 012038–012042. https://doi.org/10.1088/1757-899x/89/1/012038.

[31] J. Ribis, Y. de Carlan, Interfacial strained structure and orientation relationships of the nanosized oxide particles deduced from elasticity-driven morphology in oxide dispersion strengthened materials, Acta Mater. 60 (2012) 238–252. https://doi.org/10.1016/j.actamat.2011.09.042.

[32] Z. Zhu, W. Ji, H. Huang, In-situ TEM investigation on the evolution of he bubbles and dislocation loops in ni-based alloy irradiated by H2+ & he+ dual-beam ions, J. Mater. Sci. Technol. 138 (2023) 36–49. https://doi.org/10.1016/j.jmst.2022.07.054.

[33] L.X. Zhang, L. Liu, S. Guo, Q.S. Pan, L. Lu, Microstructure and evolution of gradient dislocation cells in multi-principal element alloy subjected to cyclic torsion, Acta Materialia 275 (2024) 120059. https://doi.org/10.1016/j.actamat.2024.120059.

[34] P. Maj, J. Zdunek, M. Gizynski, J. Mizera, K.J. Kurzydlowski, Statistical analysis of the portevin–le chatelier effect in inconel 718 at high temperature, Mater. Sci. Eng., A 619 (2014) 158–164. https://doi.org/10.1016/j.msea.2014.09.075.

[35] B. Reppich, On the attractive particle–dislocation interaction in dispersion-strengthened material, Acta Materialia 46 (1998) 61–67. https://doi.org/10.1016/S1359-6454(97)00234-6.

[36] M. He, Z. Xiang, J. Yi, Y. Ni, S. Wang, A comparison of dislocation cellular patterns generated in inconel 718 alloy and pure ni fabricated by laser powder bed fusion, Vacuum 199 (2022) 110974. https://doi.org/10.1016/j.vacuum.2022.110974.

[37] Y.M. Wang, T. Voisin, J.T. McKeown, J. Ye, N.P. Calta, Z. Li, Z. Zeng, Y. Zhang, W. Chen, T.T. Roehling, R.T. Ott, M.K. Santala, P.J. Depond, M.J. Matthews, A.V. Hamza, T. Zhu, Additively manufactured hierarchical stainless steels with high strength and ductility, Nature Mater 17 (2018) 63–71. https://doi.org/10.1038/nmat5021.

[38] W.W. Hu, Z.Q. Yang, H.Q. Ye, Cottrell atmospheres along dislocations in long-period stacking ordered phases in a Mg–Zn–Y alloy, Scripta Materialia 117 (2016) 77–80. https://doi.org/10.1016/j.scriptamat.2016.02.030.

[39] C. Krempaszky, U. Liedl, E.A. Werner, A note on the diffusion of carbon atoms to dislocations, Computational Materials Science 38 (2006) 90–97. https://doi.org/10.1016/j.commatsci.2006.01.010.

[40] T. Oyama, M. Yoshiya, H. Matsubara, K. Matsunaga, Numerical analysis of solute segregation at ∑5(310)/[001] symmetric tilt grain boundaries in Y2O3-doped ZrO2, Phys. Rev. B 71 (2005) 224105. https://doi.org/10.1103/PhysRevB.71.224105.

[41] B. Qiao, Z. Sun, Q. Jin, T. Yao, Y. Jiang, A. Tao, X. Yan, M. Tian, T. Xiong, Z. Yang, H. Ye, C. Chen, Strain-Induced Gradient Distribution of Dopants at a Perovskite Interface, Nano Lett 25 (2025) 4163–4169. https://doi.org/10.1021/acs.nanolett.4c05137.

[42] N. Hansen, Hall–Petch relation and boundary strengthening, Scripta Materialia 51 (2004) 801–806. https://doi.org/10.1016/j.scriptamat.2004.06.002.

[43] K.S. Mukhtarova, R.V. Shakhov, S.K. Mukhtarov, V.V. Smirnov, V.M. Imayev, Microstructure and mechanical properties of the Inconel 718 superalloy manufactured by selective laser melting, Lett. Mater. 9 (2019) 480–484. https://doi.org/10.22226/2410-3535-2019-4-480-484.

[44] Y.-L. Kuo, S. Horikawa, K. Kakehi, The effect of interdendritic δ phase on the mechanical properties of Alloy 718 built up by additive manufacturing, Materials & Design 116 (2017) 411–418. https://doi.org/10.1016/j.matdes.2016.12.026.

[45] D.B. Witkin, R.W. Hayes, T.D. McLouth, G.E. Bean, Anomalous Notch Rupture Behavior of Nickel-Based Superalloy Inconel 718 Due to Fabrication by Additive Manufacturing, Metall Mater Trans A 50 (2019) 3458–3465. https://doi.org/10.1007/s11661-019-05298-7.

[46] T. Trosch, J. Strößner, R. Völkl, U. Glatzel, Microstructure and mechanical properties of selective laser melted Inconel 718 compared to forging and casting, Materials Letters 164 (2016) 428–431. https://doi.org/10.1016/j.matlet.2015.10.136.

[47] V.A. Popovich, E.V. Borisov, A.A. Popovich, V.Sh. Sufiiarov, D.V. Masaylo, L. Alzina, Impact of heat treatment on mechanical behaviour of Inconel 718 processed with tailored microstructure by selective laser melting, Materials & Design 131 (2017) 12–22. https://doi.org/10.1016/j.matdes.2017.05.065.

[48] P.M. Hazzledine, Direct versus indirect dispersion hardening, Scripta Metallurgica et Materialia 26 (1992) 57–58. https://doi.org/10.1016/0956-716X(92)90368-O.